

Supporting Information for
**Boosting room-temperature thermoelectricity in
SrTiO₃ based superlattices**

Yi Zhu^{1,2}, Wenzhao Wang², Bokai Liang², Wei Liu², Tao Zhou², Biwei Meng³,
Hao Liu^{1,2}, Wenping Gao^{1,2}, Yulong Yang², Chang Niu^{1,2}, Changlin Zheng^{1,2},
Zhenhua An^{1,2,4,5}, Shiwei Wu^{1,2,4,5}, Weitao Liu^{1,2,4}, Yuqiao Zhang⁷, Chao Yuan^{3,*},
Yinyan Zhu^{1,4,5,*}, Lifeng Yin^{1,2,4,5,*} and Jian Shen^{1,2,4,5,6,*}

¹ *State Key Laboratory of Surface Physics and Institute for Nanoelectronic Devices
and Quantum Computing, Fudan University, Shanghai 200433, China*

² *Department of Physics, Fudan University, Shanghai 200433, China*

³ *The Institute of Technological Sciences, Wuhan University, Wuhan 430072, China*

⁴ *Shanghai Research Center for Quantum Sciences, Shanghai 201315, China*

⁵ *Zhangjiang Fudan International Innovation Center, Shanghai 201203, China*

⁶ *Shanghai Branch, Hefei National Laboratory, Shanghai 201315, China*

⁷ *Institute of Quantum and Sustainable Technology (IQST), School of Chemistry and
Chemical Engineering, Jiangsu University, Zhenjiang 212013, China*

*Correspondence to: Jian Shen (shenj5494@fudan.edu.cn), Lifeng Yin (lifengyin@fudan.edu.cn), Yinyan Zhu (zhuyinyan@fudan.edu.cn) and Chao Yuan (chaoyuan@whu.edu.cn).

Materials and Methods:

Sample preparation.

High quality [(STO)_x/(Nb-STO)₃]₁₀ ($x=3, 6, 9$) superlattices were grown on the insulating DSO (110) single-crystal substrates (pseudo-cubic perovskite, the surface area: 1 cm × 1 cm) by laser molecular beam epitaxy with a KrF excimer laser (248 nm, 5 Hz, 1 J/cm⁻²). The growth conditions were precisely controlled; the substrate temperature was 800 °C, the oxygen pressure was 8×10⁻⁵ Torr. The thicknesses of different layers were monitored in situ using the intensity oscillation of the RHEED spots.

Crystallographic analyses of the superlattices.

Crystallographic analyses of the superlattices were performed by XRD (Cu K α 1, D8 Discover, Bruker) and AFM (NX10, Paker system). Synchrotron XRD measurements were carried out at beamline BL02U2 of Shanghai Synchrotron Radiation Facility at room temperature, using 9.8 keV X-rays (1.2651 Å).

STEM measurements.

TEM cross-sectional samples were fabricated using a Focused Ion Beam (FIB, Helios G4, FEI). The STEM, EDS and EELS investigations were conducted using a double aberration-corrected field emission STEM (Themis Z, Thermo Fisher Scientific) operated at 300 kV. The microscope is equipped with a SCORR probe corrector and a Super-X EDS detector. HAADF images were recorded with a probe semi convergent angle of 21.4 mrad, and a collection angle 76-200 mrad. EDS experiments were conducted with a probe current of 150 pA. STEM-EELS data was collected with a Gatan continuum 1066/HR GIF system. The EELS energy resolution (FWHM of zero loss peak) is 0.9 eV.

Measurements of the electrical and thermoelectrical properties.

Electrical conductivity (σ), carrier concentration (n_e), and Hall mobility (μ_{Hall}) were measured at room temperature by a conventional d.c. four-probe method with a van der Pauw geometry in the physical property measurement system (PPMS, Quantum Design).

Seebeck coefficient (S) was measured by thermoelectric parameter test system (MRS-3, JouleYacht). The Seebeck potential (ΔV) and Temperature difference (ΔT) were measured simultaneously, and the S values were obtained from the slope of the ΔV – ΔT plots.

Measurements of the thermal conductivity.

The nanosecond transient thermoreflectance (TTR) technique was used to characterize the thermal properties of [(STO)₉/(Nb-STO)₃] superlattices (SLs), STO and Nb-STO thin films. The schematic of the TTR measurement is shown in Supplementary Fig. S4. Prior to TTR thermal measurements, a ~71 nm Au transducer and ~2 nm Cr adhesion layer were deposited on the sample surfaces by thermal evaporation. The pump beam is a 3.2 ns, 355 nm pulsed laser with a 10.8 kHz repetition rate. After passing through a beam expander and dichroic beam splitter, it is directed through a 15 × objective to a de-focused spot on the sample surface with a Gaussian profile. The transient surface reflectivity change is monitored using a CW 532 nm laser probe beam focused at the sample surface in the central location of the pump spot. At 532 nm wavelength, the Au exhibits a reflectance change directly and linearly related to temperature change within a large temperature range, ensuring the most fundamental basis of the thermoreflectance techniques^{1,2}. The reflected beam intensity is sampled by a beam splitter and detected directly through a photodetector (400 MHz bandwidth) and a digital oscilloscope (500 MHz bandwidth). To ensure no residual light from the pump beam is detected, a long-pass filter is placed before the detector. The

pump and probe lasers incident on the Au transducer have a Gaussian distribution with a $1/e^2$ radius of 62 μm and 3.5 μm respectively, measured by a beam profiler (BP209-VIS, Thorlabs). To measure the thermal properties of the samples at different temperatures (175-295 K), the samples were mounted on a high accuracy microscopic thermostatic stage (Linkam THMS600). For each sample at each temperature, at least 5 points have been measured. More details on the TTR system were also reported in the previous work¹⁻⁵. The measured TTR transients were fitted by a multilayer analytical thermal transport model to extract the thermal properties of interest (i.e., thermal conductivity of epitaxial thin-films and thermal boundary conductance at each interface). The detailed procedures for the TTR fitting are provided in the supplementary notes of Supporting information.

SHG Measurements.

The SHG measurements were conducted in a variable-temperature optical cryostat. 10mW, 900nm excitation femtosecond laser pulses from a 80MHz Ti: sapphire oscillator (MaiTai HP, Spectra Physics) were used. The laser pulses were focused onto the sample at normal incidence using a microscope objective lens (Nikon, x20/NA0.45). The reflected SHG signal was collected by the same objective and detected by a photomultiplier tube in photon-counting mode. The excitation laser pulses were linear polarized and no polarizer was used for collecting SHG signal.

Uncertainty analysis of electronic and thermal transport measurements.

1. Electrical conductivity (σ) was measured at room temperature by a conventional d.c. four-probe method with a van der Pauw geometry. From the measured value of resistance R and sample dimensions (thickness d , distance between the voltage leads L and the sample length w), the electrical conductivity σ is given by

$$\sigma = \frac{L}{Rdw}.$$

We eliminated the geometric factors of the sample's symmetry by measuring with

positive and negative voltages applied in different directions of the sample⁶⁻⁸, resulting

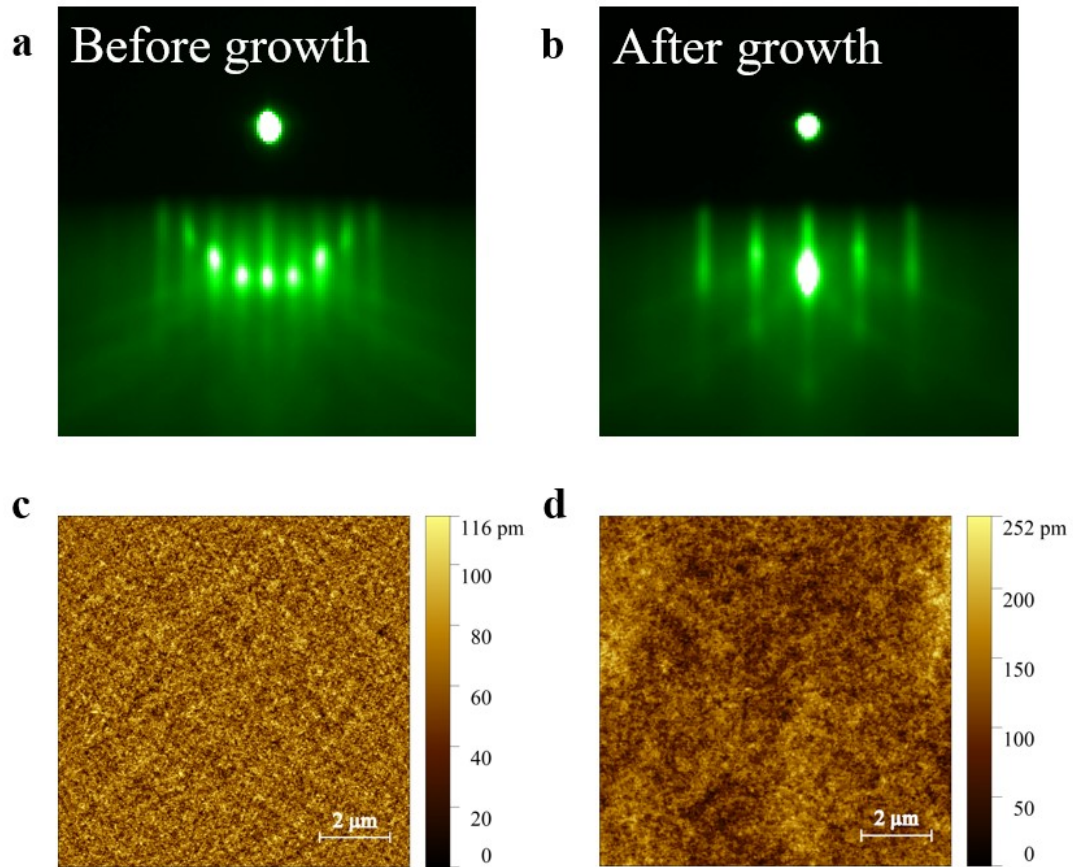
$$\sigma = \frac{1}{Rd}$$

The percentage uncertainty in σ is given as $\frac{\nabla\sigma}{\sigma} = \sqrt{\left(\frac{\nabla d}{d}\right)^2 + \left(\frac{\nabla R}{R}\right)^2}$, where $\frac{\nabla d}{d}$ and $\frac{\nabla R}{R}$ is the uncertainty of the thickness and resistance of the sample respectively. Here, $\frac{\nabla d}{d}$ is

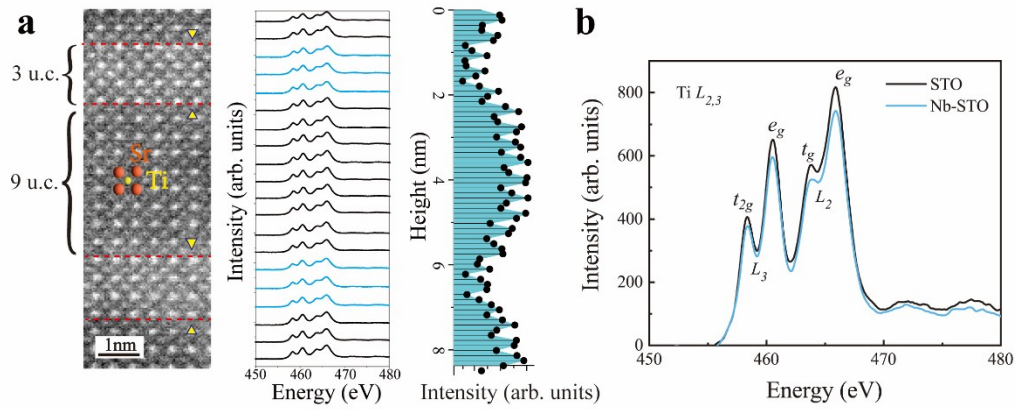
$\pm 0.5\%$ according to the growth technique and $\frac{\nabla R}{R}$ is $\pm 0.05\%$ according to the measurement accuracy of Source Meter Keysight B2902B. After taking all these errors into account, the total error of the electrical conductivity is estimated to be $\pm 0.5\%$.

2. The Seebeck potential (ΔV) and Temperature difference (ΔT) were measured simultaneously, and the S values were obtained from the slope of the ΔV - ΔT plots, as shown in Supplementary Fig. S3. The average correlation coefficient is 0.998, close to the values in previous work⁷⁻⁹. Our films are enough large (10 mm \times 10 mm) to measure the thermopower. We could add temperature difference more than ± 7 K and obtained quite a nice linearity of 0.998, which means that measurement error is negligibly small ($\pm 0.4\%$).

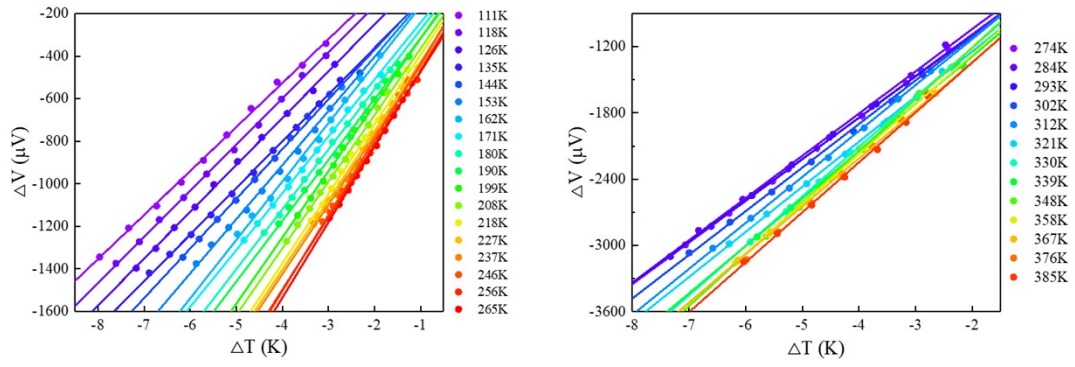
3. The thermal conductivity of superlattices was characterized by the nanosecond transient thermoreflectance (TTR) technique. The uncertainty of thermal conductivity of superlattices is $\pm 16.0\%$ at room temperature and the detailed uncertainty analysis is shown in the Supplementary notes S1.3.



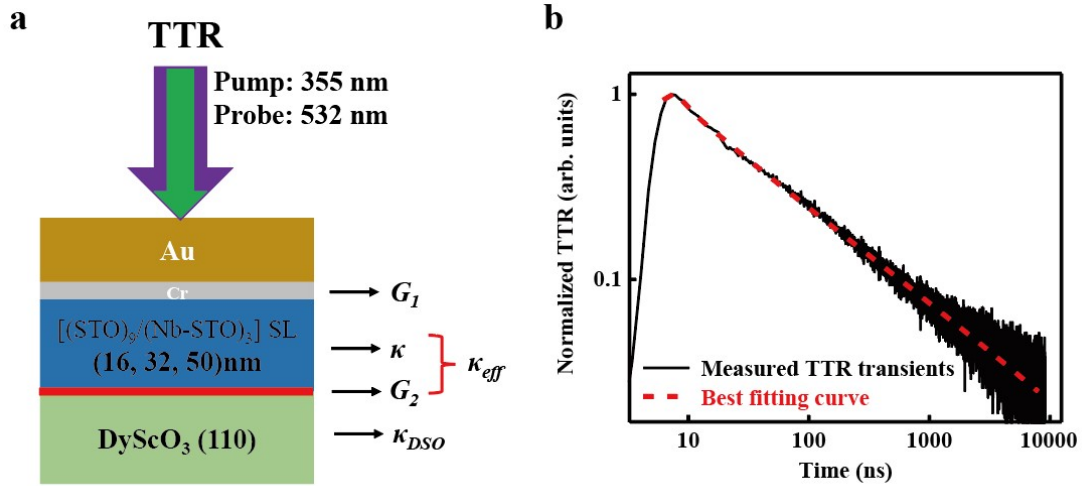
Supplementary Fig. S1: Morphology of the superlattices. The RHEED pattern of (a) DSO (110) substrate and (b) after growth of the [(STO)₉/(Nb-STO)₃]₁₀ superlattice. The AFM images of (c) the DSO (110) substrate and (d) the [(STO)₉/(Nb-STO)₃]₁₀ superlattice. The surface roughness of the superlattice is measured to be 1.5 Å.



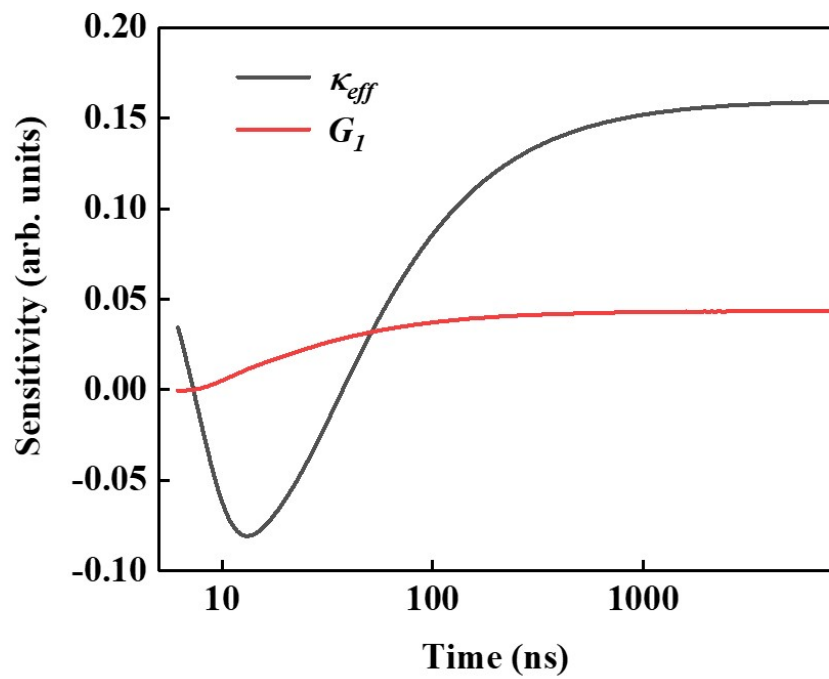
Supplementary Fig. S2: Microstructure of the superlattices. (a) STEM-ADF imaging and the corresponding EELS analysis of the $[(\text{STO})_9/(\text{Nb-STO})_3]_{10}$ superlattice. Left: ADF reference image; Middle: Layer-by-layer analysis of Ti $L_{2,3}$ spectrum; Right: Integrated intensity of Ti $L_{2,3}$ edge (456.6 – 469.6 eV) across different layers. (b) Comparison of the normalized EELS signal from the undoped-STO (black curve) region and the Nb-STO (blue curve) region. The Ti $L_{2,3}$ intensity in Nb-STO is weaker than that in undoped-STO region, suggesting that Nb substituted Ti in the Nb-STO layer.



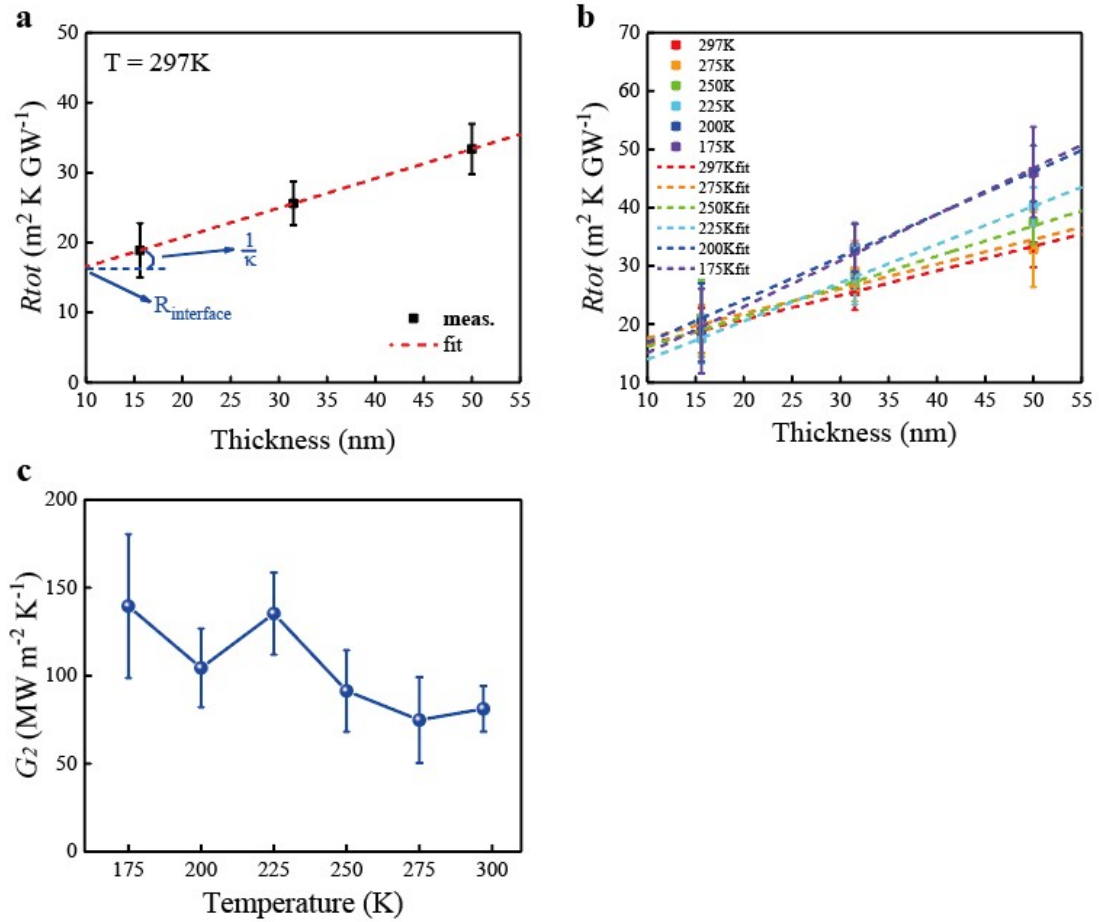
Supplementary Fig. S3: Seebeck potential versus temperature difference at different temperature. The slopes of different lines represent the Seebeck coefficients at different temperatures. The curves are linearly fits to the data.



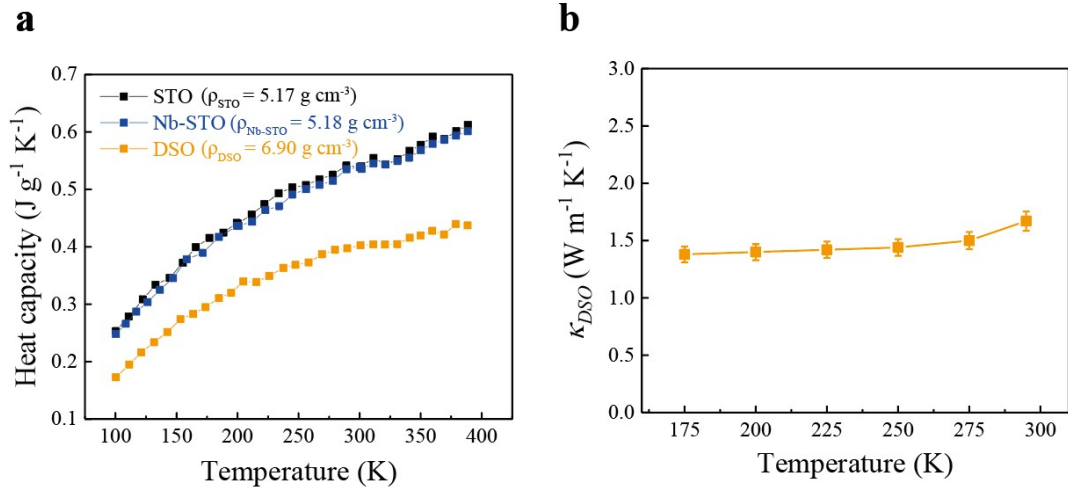
Supplementary Fig. S4: Schematic diagram of transient thermoreflectance (TTR) thermal conductivity measurements. (a) Schematic of the TTR and thermal model. (b) TTR signal for a representative sample {Au/Cr - [(STO)₉/(Nb-STO)₃] SL (50 nm) - DSO} measured at room temperature and the associated best fitting.



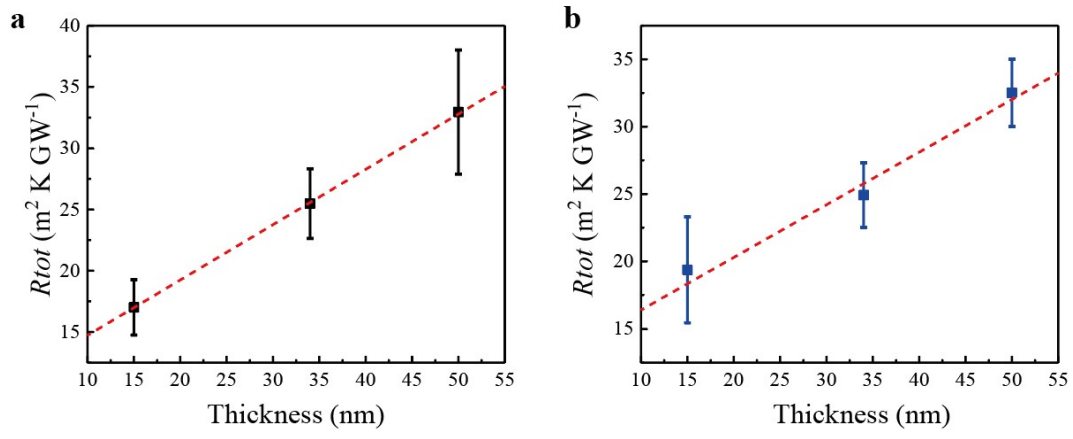
Supplementary Fig. S5: Sensitivity of the normalized TTR transient to κ_{eff} and G_1 for a representative sample {Au/Cr- [(STO)₉/(Nb-STO)₃] SL (50 nm)-DSO}.



Supplementary Fig. S6: Calculation of thermal conductivity. (a) Thickness-dependent thermal resistance for the $[(\text{STO})_9/(\text{Nb-STO})_3]$ superlattice grown on DSO (110) at room temperature. (b) Thickness-dependent thermal resistance for the $[(\text{STO})_9/(\text{Nb-STO})_3]$ superlattice at different temperatures. (c) Temperature-dependent thermal boundary conductance at the superlattice/substrate interfaces (G_2) was obtained from the intercepts in S6(b).

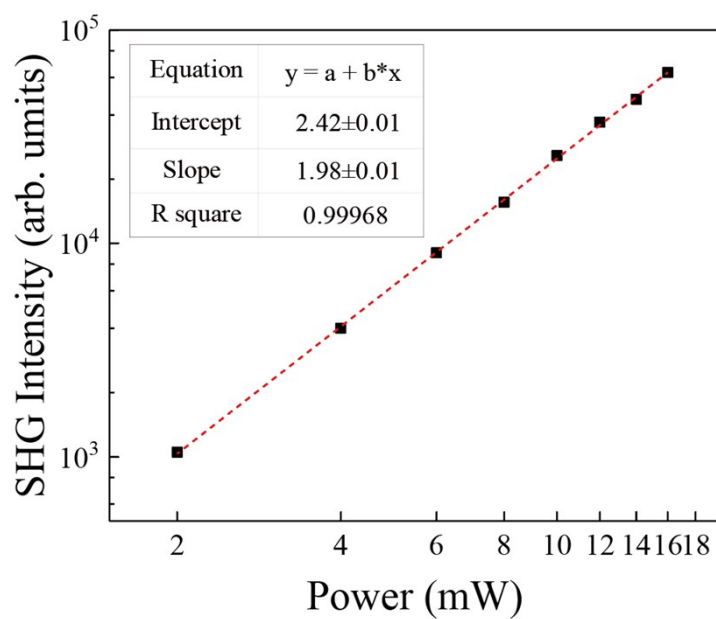


Supplementary Fig. S7: Measured temperature-dependent heat capacity and thermal conductivity. (a) The heat capacity data of DSO, STO and Nb-STO, measured by DSC, is plotted by yellow, black and blue squares, respectively. (b) Temperature-dependent thermal conductivity of DyScO₃ substrate measured by TTR.

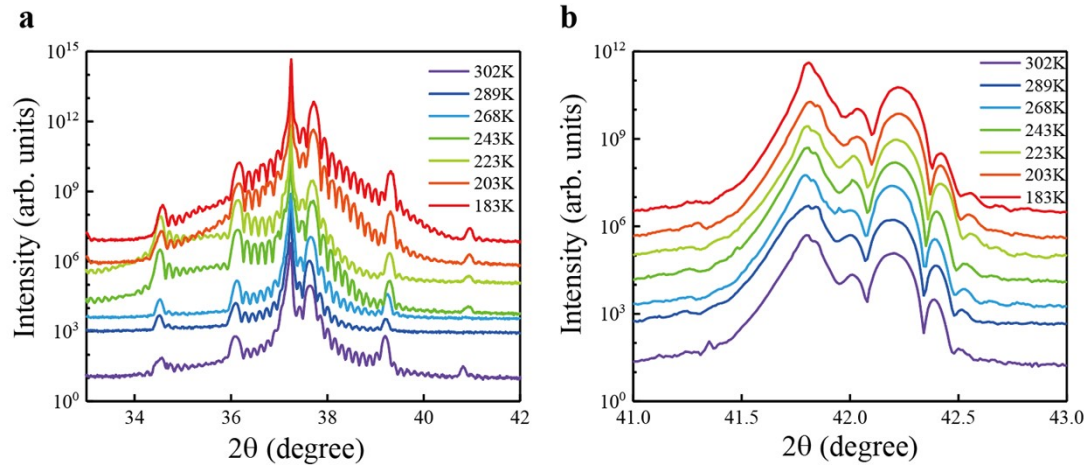


Supplementary Fig. S8: Thermal conductivity of pure STO and Nb-STO.

Thickness-dependent thermal resistance for (a) STO (b) Nb-STO films fabricated on DSO (110).



Supplementary Fig. S9: Power-dependent SHG intensity. The SHG intensity data is plotted by black squares, with its fitting data by red line. The slope of line (~ 2) indicates the intensity data is the real second harmonic signal.



Supplementary Fig. S10: Temperature-dependent X-ray diffraction. (a) High resolution short angular-range θ - 2θ XRD scan of a superlattice centered on the DSO (220) substrate peak at different temperature. (b) High resolution short angular-range θ - 2θ XRD scan of a superlattice centered on the DSO (222) substrate peak at different temperature.

Supplementary notes: Thickness-extrapolation method, TTR

Fitting and uncertainty analysis in TTR measurement

As shown in Supplementary Fig. S4(a), the essential structural components of the Au-Cr coated [(STO)₉/(Nb-STO)₃] superlattice (SL) samples, from top to bottom, include Au, the interface between Au and [(STO)₉/(Nb-STO)₃] SL, the [(STO)₉/(Nb-STO)₃] SL, the interface between [(STO)₉/(Nb-STO)₃] SL and DSO substrate, and the DSO substrate. Due to the ultrathin-film nature of the [(STO)₉/(Nb-STO)₃] SL film (< 50 nm), TTR signal are sensitive to both interfaces and the [(STO)₉/(Nb-STO)₃] SL film sandwiched in between, and the sensitivity to each parameter overlaps severely. This leads to a challenge in direct fitting of TTR signal to simultaneously extract the thermal conductivity of the [(STO)₉/(Nb-STO)₃] SL (κ), as well as the thermal boundary conductance at the Au-[(STO)₉/(Nb-STO)₃] SL interface (G_1) and [(STO)₉/(Nb-STO)₃] SL/substrate (G_2) interfaces. In this work, a thickness-extrapolation method was used to quantify the κ , G_1 and G_2 .

S1.1 Thickness-extrapolation method

If the characteristic time for heat diffusion in the sample (t^2/α , where t and α are the film thickness and thermal diffusivity, respectively) is much shorter than the timescale of thermoreflectance transients, the temperature profile in the film can be approximated by a steady-state one-dimensional (1D) solution along its thickness^{10,11}. In this limit, the contribution of the thermal resistance of the thin film and thermal boundary conductance at film-substrate can be added to obtain the total thermal resistance,

$$\frac{t}{\kappa_{eff}} = \frac{t}{\kappa} + \frac{1}{G_2} \quad (S1)$$

κ and t and the thermal conductivity and thickness of the [(STO)₉/(Nb-STO)₃] SL thin-film, respectively, and G_2 is thermal boundary conductance at [(STO)₉/(Nb-STO)₃] SL/substrate interface, κ_{eff} is the effective thermal conductivity combining the contributions from the [(STO)₉/(Nb-STO)₃] SL film and G_2 . Thus, $1/\kappa$ and $1/G_2$ can be

$\frac{t}{\kappa_{eff}}$ obtained from the slope of $\frac{t}{\kappa_{eff}}$ vs t and the intercept at zero film thickness, respectively, measured for a series of samples of different thicknesses. Therefore, we grew three different films with thicknesses of 16 nm, 32 nm and 50 nm on the same DyScO₃ substrate under identical conditions. Here, this extrapolation method assumes that κ and G_2 are not thickness dependent. G_2 is presumed thickness independent for these series of films on the same substrate, as justified by the identical deposition conditions.

Increases in κ with thickness would register as nonlinear, concave down $\frac{t}{\kappa_{eff}}$ vs t , which we do not observe. The good fitting to Eq. (S1) [shown in Supplementary Fig. S6(a)] validates the steady-state 1D approximation, and justifies the validity of this thickness-extrapolation method. Despite this, κ extracted from Eq. (S1) is treated here as an apparent value, averaged over epitaxial films on the same substrate with varying thicknesses (16–50 nm).

This measurement strategy is essential the same as that reported in previous literature¹⁰⁻¹². Slight modification to the approach in our work is that G_l is not included in Eq. (1) so that G_l is fitted simultaneously with κ_{eff} (see the details in Section S1.2).

This modification is made for the reason that: G_I is not the discrete thermal boundary conductance but rather an effective conductance involving multiple contributions: thermal boundary conductance at Au/Cr interface, electron-phonon coupling thermal conductance of Cr interlayer and thermal boundary conductance at Cr/SL interface; slight variation in interlayer (Cr)'s quality and thickness could significantly alter this lumped thermal conductance (G_I)¹³⁻¹⁶. The uniformity of Cr quality and thickness across the sample surface is hard to be ensured in our thermal evaporation metal coating system. Therefore, the assumption of thickness independence is not likely reasonable for G_I . Table S1 also confirms that the G_I is not identical in different samples.

S1.2 Transients fitting

Fig. S4(b) provides the TTR signal for a representative sample {Au/Cr-[(STO)₉/(Nb-STO)₃] SL (50 nm)-DSO} measured at room temperature and the associated best fitting. In the fitting, K_{eff} and G_I were considered as free variables and the rest of the parameters were the controlled parameters which were determined by separate measurements or from literature. The thickness of the Au/Cr layer (~71 nm/~2nm) was measured by the profilometer, and that of [(STO)₉/(Nb-STO)₃] SL film was determined by XRD. The Au density was taken as 19300 kg m⁻³¹⁷, temperature-dependent specific heat capacity and thermal conductivity were from previous work^{18,19}. A four-probe technique was also used to determine the thermal conductivity of Au at room temperature, which was consistent with the reported values¹⁹. The density of STO and Nb-STO were taken from chemical formula²⁰. Temperature-dependent specific heat capacities of STO, Nb-STO and DSO were measured by DSC (Differential

Scanning Calorimetry), and provided in Fig. S7(a), respectively. Temperature-dependent thermal conductivity of DSO substrate, shown in Fig. S7(b), was obtained from a separate TTR measurement of a bare DSO, the same as that used for [(STO)₉/(Nb-STO)₃] SL growth.

The above fitting procedure applies for the [(STO)₉/(Nb-STO)₃] SLs with different thicknesses, obtaining κ_{eff} and G_I for each sample. Table S1 summarizes the fitted κ_{eff} and G_I for the three samples at room temperature. For each sample, G_I varies between a relatively large range, whereas κ_{eff} varies much less. This finding could be explained by sensitivity analysis. The sensitivity (Sx_i) of normalized TTR transient (H) at any point of time (t) to parameter x_i is defined as^{1,2,21,22}:

$$Sx_i = \frac{\partial(\ln H)}{\partial(\ln x_i)} \quad (S2)$$

When x_i changes by $\pm 10\%$,

$$Sx_i = \frac{\partial(\ln H)}{\partial(\ln x_i)} \approx \frac{(\ln H_{1.1 * x_i} - \ln H_{0.9 * x_i})}{\ln(1.1 * x_i) - \ln(0.9 * x_i)} \quad (S3)$$

where x_i is either κ_{eff} and G_I . The sensitivity plot (Fig. S5) confirms that the measurement sensitivity is more reasonable for κ_{eff} than G_I . The low sensitivity to G_I results in a low fitting accuracy of G_I . However, the determination of κ_{eff} is not significantly impacted by G_I , as seen in the results in Table S1.

Table S1 The effective thermal conductivity and interface thermal conductance at different measured areas.

Sample	Location	κ_{eff} (W/mK)	G_I (MW/m ² K)
50 nm SL	1	1.37	95
	2	1.78	233

	3	1.63	276
	4	1.48	347
	5	1.32	251
	6	1.49	268
	Average	1.51	246
	Standard deviation	0.17	83
34 nm SL	1	1.35	493
	2	1.11	277
	3	1.55	248
	4	0.83	410
	5	1.39	302
	6	1.32	385
	Average	1.34	353
	Standard deviation	0.25	158
15 nm SL	1	1.20	415
	2	0.78	459
	3	0.68	373
	4	0.69	300
	5	0.79	319
	Average	0.83	373
	Standard deviation	0.22	66

Fig. S6(a) plots $\frac{t}{\kappa_{eff}}$ as function t . Based on the extrapolation method, a linear fit was then applied for the data with a slope $1/\kappa$ and a vertical axis intercept $1/G_2$. Thus, both κ and G_2 can be measured. This procedure was repeated for every temperature analysed in this paper, as shown in Fig. S6(b). The measured T -dependent κ of [(STO)₉/(Nb-STO)₃] SL was shown in Fig. 3c of main text, and the T -dependent G_2 was shown in Fig. S6(c).

The same TTR characterizations were also carried on the STO and Nb-STO thin films at room temperature. 15 nm, 34 nm and 50 nm of STO films were grown on the DSO substrate. The Nb-STO films were grown with the same conditions and

thicknesses. Fig. S8 plots the linear fit for the obtained $\frac{t}{\kappa_{eff}}$ v.s. t for STO and Nb-STO, respectively, whereby κ of these two films are obtained.

S1.3 Uncertainty analysis

The κ was extracted through linear regression by Eq. (S1), and its uncertainty should take into account the standard deviation of the data points to the fitted straight line, as well as the uncertainty associated with each $y_i = t/\kappa_{eff}$ measurement. The uncertainty of $y_i = R_{eff} = t/\kappa_{eff}$ at each data point can be obtained by

$$\frac{\nabla R_{eff}}{R_{eff}} = \sqrt{\left(\frac{\nabla t}{t}\right)^2 + \left(\frac{\nabla \kappa_{eff}}{\kappa_{eff}}\right)^2} \quad (S4)$$

where $\frac{\nabla t}{t}$ is the uncertainty of thickness of the epitaxial [(STO)₉/(Nb-STO)₃] SLs, and $\frac{\nabla \kappa_{eff}}{\kappa_{eff}}$ is the uncertainty of κ_{eff} . $\frac{\nabla t}{t}$ is 0.5% according to the growth technique; $\frac{\nabla \kappa_{eff}}{\kappa_{eff}}$ can be estimated by Monte Carlo error analysis, which is routinely used for calculate uncertainty of fitting parameters in TTR measurements^{2,3,23}. The controlled parameters described in TTR fitting section (S1.2) are assumed to have a normal distribution around its mean value with an uncertainty (2σ , 95% confidence level). The same set of transients was then repeatedly fitted by the analytical model 1000 times with the controlled parameters randomly selected from their distribution, yielding new distributions of the fitted parameters. The uncertainties of the fitted parameters could thus be determined from the 2σ of their distributions. For the Au-Cr coated [(STO)₉/(Nb-STO)₃] SLs on DyScO₃ samples, the Monte Carlo error analysis accounts for the uncertainty in Au thickness ($\pm 5\%$), thermal conductivity ($\pm 2\%$) and specific

heat ($\pm 2\%$), [(STO)₉/(Nb-STO)₃] SL thickness ($\pm 0.5\%$) and specific heat ($\pm 2\%$), DyScO₃ thermal conductivity ($\pm 5\%$) and specific heat ($\pm 2\%$), and spot size ($\pm 3\%$). The uncertainties of κ_{eff} and G_1 calculated by the MC analysis are about $\pm 16\%$ and $\pm 80\%$ for the [(STO)₉/(Nb-STO)₃] SLs samples at all temperatures. The large error bar obtained in G_1 is as expected since the sensitivity to G_1 is very low. However, the uncertainties of κ_{eff} is not significantly impacted by the poor measurement uncertainty of G_1 . After the uncertainties of κ_{eff} is obtained, the uncertainty associated with $y_i = t/\kappa_{eff}$ measurement can be determined according to Eq. (S4). Table S2 summarizes the κ and G_2 total uncertainties (u_{tot}) contributed by the standard deviation of the fitted straight line (u_{fit}) and the uncertainty associated with $y_i = t/\kappa_{eff}$ measurement (u_{eff}), respectively. Similar error analysis was conducted for determining the uncertainty of κ of STO and Nb-STO, where both standard deviation of the fitted straight line and the uncertainty associated with each $y_i = t/\kappa_{eff}$ measurement were considered. It should be noted that we provide a conservatively large estimation for the uncertainty in the κ and G_2 . The error analysis approach that we used is essential the same as that published in the paper¹¹.

Table S2 The uncertainty of thermal conductivity and interface thermal conductance

T	κ			G_2		
	$u_{fit}(\kappa)$	$u_{eff}(\kappa)$	$u_{tot}(\kappa)$	$u_{fit}(G_2)$	$u_{eff}(G_2)$	$u_{tot}(G_2)$
295 K	$\pm 0.1\%$	$\pm 16.0\%$	$\pm 16.0\%$	$\pm 0.2\%$	$\pm 16.0\%$	$\pm 16.0\%$
275 K	$\pm 29.4\%$		$\pm 33.5\%$	$\pm 28.5\%$		$\pm 32.7\%$

250 K	± 12.3%	± 20.2%	± 19.7%	± 25.4%
225 K	± 1.9%	± 16.1%	± 6.4%	± 17.2%
200 K	± 5.0%	± 16.8%	± 14.2%	± 21.4%
175 K	± 6.6%	± 17.3%	± 24.5%	± 29.3%

Supplementary References:

- 1 C. Yuan, R. Hanus and S. Graham, *Journal of Applied Physics*, 2022, **132**, 220701.
- 2 B. W. Meng, Y. L. Ma, X. H. Wang and C. Yuan, *Journal of Applied Physics*, 2023, **134**, 115102.
- 3 Y. M. Wang, B. Zhou, G. L. Ma, J. Q. Zhi, C. Yuan, H. Sun, Y. Ma, J. Gao, Y. S. Wang and S. W. Yu, *Materials Characterization*, 2023, **201**, 112985.
- 4 G. Ma, Y. Wang, R. Xia, B. Meng, S. Yuan, B. Zhou and C. Yuan, *Diamond and Related Materials*, 2024, **141**, 110717.
- 5 X. L. Xiao, Y. L. Mao, B. W. Meng, G. L. Ma, K. Huseková, F. Egyenes, A. Rosová, E. Dobrocka, P. Elias, M. Tapajna, F. Guemann and C. Yuan, *Small*, 2023, 2309961.
- 6 Z. Zhou and C. Uher, *Review of Scientific Instruments*, 2005, **76**.
- 7 J. Mackey, F. Dynys and A. Sehirlioglu, *Review of Scientific Instruments*, 2014, **85**, 085119.
- 8 L. Sun, B. Liao, D. Sheberla, D. Kraemer, J. Zhou, E. A. Stach, D. Zakharov, V. Stavila, A. A. Talin, Y. Ge, M. D. Allendorf, G. Chen, F. Léonard and M. Dincă, *Joule*, 2017, **1**, 168-177.
- 9 Y. Q. Zhang, B. Feng, H. Hayashi, C. P. Chang, Y. M. Sheu, I. Tanaka, Y. Ikuhara and H. Ohta, *Nature Communications*, 2018, **9**, 2224.
- 10 A. Sarantopoulos, D. Saha, W. L. Ong, C. Magen, J. A. Malen and F. Rivadulla, *Physical Review Materials*, 2020, **4**, 054002.
- 11 X. W. Wu, J. Walter, T. L. Feng, J. Zhu, H. Zheng, J. F. Mitchell, N. Biskup, M. Varela, X. L. Ruan, C. Leighton and X. J. Wang, *Advanced Functional Materials*, 2017, **27**, 1704233.
- 12 M. D. Losego, L. Moh, K. A. Arpin, D. G. Cahill and P. V. Braun, *Applied Physics Letters*, 2010, **97**, 011908.
- 13 M. Y. Jeong, J. P. Freedman, H. J. Liang, C. M. Chow, V. M. Sokalski, J. A. Bain and J. A. Malen, *Physical Review Applied*, 2016, **5**, 014009.
- 14 M. Blank, G. Schneider, J. Ordonez-Miranda and L. Weber, *Journal of Applied Physics*, 2019, **126**, 165302.
- 15 H. T. Aller, J. A. Malen and A. J. H. McGaughey, *Physical Review Applied*, 2021, **15**, 064043.
- 16 M. Blank and L. Weber, *Journal of Applied Physics*, 2018, **124**, 105304.
- 17 F. Habashi, in *Encyclopedia of Metalloproteins*, eds. R. H. Kretsinger, V. N. Uversky and E. A. Permyakov, Springer New York, New York, NY, 2013, pp. 932-933.
- 18 B. Feng, Z. X. Li and X. Zhang, *Thin Solid Films*, 2009, **517**, 2803-2807.
- 19 Y. Takahashi and H. Akiyama, *Thermochimica Acta*, 1986, **109**, 105-109.
- 20 I. Border Blue, *Journal*, 2023.
- 21 C. Yuan, J. H. Li, L. Lindsay, D. Cherns, J. W. Pomeroy, S. Liu, J. H. Edgar and M. Kuball, *Communications Physics*, 2019, **2**, 43.
- 22 C. Yuan, W. M. Waller and M. Kuball, *Review of Scientific Instruments*, 2019, **90**, 114903.
- 23 C. Yuan, B. W. Meng, Y. L. Mao, M. Wu, F. C. Jia, L. Yang, X. H. Ma and Y. Hao,

Acs Applied Electronic Materials, 2022, **4**, 5984-5995.